Materials & Design 235 (2023) 112393

Contents lists available at ScienceDirect

Materials & Design

journal homepage: www.elsevier.com/locate/matdes

Revolutionary auxetic intravascular medical stents for angioplasty applications

Mohammad Sadegh Ebrahimi [a], Mohammad Noruzi [a], Ramin Hamzehei [b], Ehsan Etemadi [c,d], Ramin Hashemi [a,*]

[a] School of Mechanical Engineering, Iran University of Science and Technology, Tehran, Iran
[b] Department of Mechanical Engineering, University of Manitoba, Winnipeg, Canada
[c] Institute of Textile and Clothing, The Hong Kong Polytechnic University, Hong Kong, China
[d] Department of Mechanical Engineering, Hakim Sabzevari University, Sabzevar, Iran

ARTICLE INFO

Keywords:
Metamaterials
Auxetic stents
3D printing
Angioplasty
Artery damage
Load bearing capacity
Recoil percentage

ABSTRACT

Due to the significant mortality rate associated with atherosclerosis-induced cardiovascular disease, the utilization of advanced intravascular stents with superior mechanical performance is imperative for the restoration of obstructed arteries. This study proposes novel auxetic medical stents that aim to enhance critical parameters of biomedical stents. This includes load-bearing capacity, expanded opening percentage, and reduced recoil percentage. On this matter, the missing rib auxetic unit cell has been considered and geometrically modified to achieve these objectives. Two-dimensional (2D) metamaterials were fabricated through additive manufacturing technique and subjected to experimental testing. Then, finite element analysis (FEA) was employed to gain comprehensive insights into the mechanical behaviour of the proposed medical stents. Remarkably, an excellent correlation was observed between the FEA and experimental results, validating the high precision of the analysis. The findings reveal that the stents classified as "E-category" exhibit the highest final opening percentage while concurrently demonstrating the lowest recoil percentage. The base stent exhibited a relatively high recoil percentage of 15.56%, indicating a significant amount of recoil or spring-back after deformation. In contrast, the modified "E-category" stent displayed a substantially lower recoil percentage of 1.62%. This notable reduction in recoil percentage indicates that the modifications made to the rib-unit cells had a significant and beneficial effect on the stent's recoil behaviour and minimizing potential damage to arterial tissue during stent deployment (angioplasty) and balloon pressure. The modified design likely enhances the stent's ability to maintain its shape and resist recoil, making it more effective and reliable in its intended application. Additionally, more aspects of biomedical stents such as foreshortening, and dog-boning of the modified missing rib stents were meticulously examined through FEA.

1. Introduction

Coronary artery disease occurs due to plaque buildup on the inner surface of an artery, which narrows and blocks in the advanced stages of the disease. As a result of the hardening of the arteries, atherosclerosis occurs. Smoking, high-fat diets, inactivity, and aging are all factors that contribute to obstructive diseases, such as atherosclerosis [1]. The progression of medical device technology has led to stent placement becoming one of the primary treatment options for coronary artery disease. The stent is a small, expandable tube placed inside narrowed arteries to restore the flow of oxygen-rich blood through arteries, thus enabling the normal functioning of the heart. Stents can be classified by their clinical application or design and engineering features, including materials, coatings, geometry, and fabrication method. Stent materials determine their permanent or biodegradable nature and their expansion methods, which are self-expanding or balloon-expandable [2].

Even though stents provide many medical applications and benefits, they may also provide many disadvantages. During radial expansion, axial shrinkage is known as foreshortening [3]. A phenomenon known as dog-boning [3–6] occurs when the stent's ends are more expanded than its middle, resulting in a bone-shaped configuration. Stent migration is the movement of a stent after deployment [4,5,7,8]. Restenosis

* Corresponding author.
E-mail address: rhashemi@iust.ac.ir (R. Hashemi).

https://doi.org/10.1016/j.matdes.2023.112393
Received 25 July 2023; Received in revised form 28 September 2023; Accepted 6 October 2023
Available online 7 October 2023

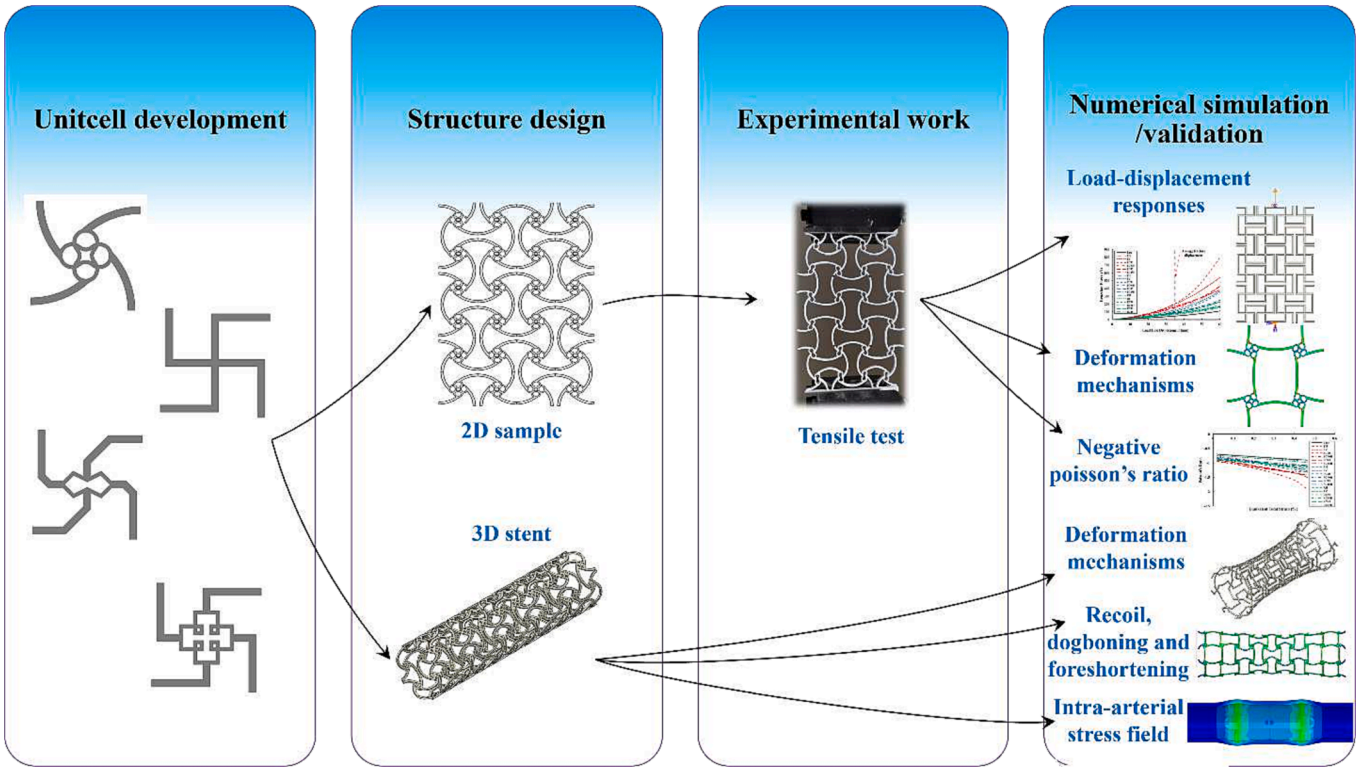

Fig. 1. Workflow of the current study.

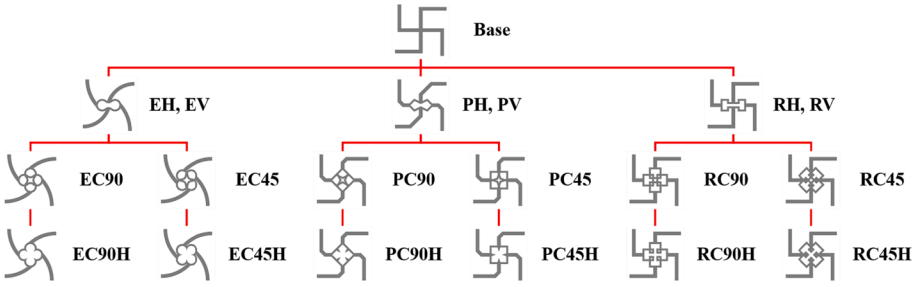

Fig. 2. The development plan for the missing rib unit cells.

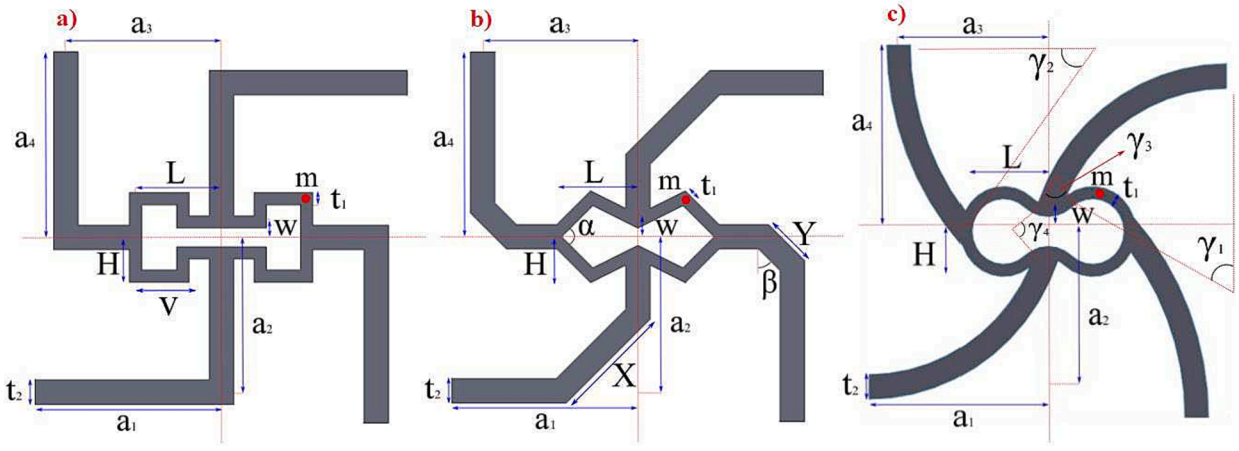

Fig. 3. Unit cells geometry modifications: (a) Rectangular, (b) Pentagonal, (c) Elliptical.

Table 1
The value of the geometric ratios.

Parameter	$z_1 = \frac{t_2}{t_1}$	$z_2 = \frac{L}{t_1}$	$z_3 = \frac{L}{W}$	$z_4 = \frac{L}{H}$	$z_5 = \frac{V}{W}$	$z_6 = \frac{X}{L}$	$z_7 = \frac{X}{Y}$
Value	2	6.875	5.5	2.2	3	0.6	2.33

Table 2
The values of the geometric angles.

Parameter	α	β	γ_1	γ_2	γ_3	γ_4
Value (Degree)	90	45	71.5	41.1	83.6	96.3

describes re-narrowing the lesion after stenting. Additionally, thrombosis [4,8,9], stent collapse [7,8], and isotropic properties [6,8] are discussed.

The mechanical behavior of a stent under various loading conditions, such as tensile, compression, bending, and crushing, plays a vital role in the functionality of the stent, including structural support, blood flow adjustments, drug delivery efficiency improvement, and so forth. The ideal stent would be one that can reopen narrowed vessels with large radius expanding deformation, have high radial strength [5] for good arterial support post-expansion, adequate flexibility [10], biocompatibility, biodegradability, cause minimal injury to the artery in an expanded state, and result in a small amount of axial recoil for minimal shear damage [11,12]. Additionally, there is inevitably a trade-off between radial strength and bending flexibility in stent design [10].

The mechanical properties of stents are crucial for the successful recovery of blood vessels. In this regard, artificially designed structures, so-called mechanical metamaterials, could significantly enhance stent mechanical properties. These structures divide into several main groups, including positive Poisson's ratio (PPR), zero Poisson's ratio (ZPR) [13–15], and negative Poisson's ratio (NPR) [16]behavior. Amongst those lattices, NPR structures, so-called auxetics have been proposed to improve radial expansion abilities and reduce axial expansion [17–20]. Auxetic structures represent an NPR behaviour when subject to mechanical loads [21,22]. This behavior is due to the architectural design rather than the material composition [23]. Stents with a ZPR or NPR behavior can reduce foreshortening and dog-boning effects in balloon-expandable coronary stents [3].

Additionally, auxetic behavior, so-called auxeticity, can improve the mechanical performance of stenting, prevent stent fractures, enhance the stent's fatigue resistance, and ultimately decrease its risk of failure [24]. Several body tissues and organs exhibit auxeticity, including bone marrow [25], the membranes that make up the red blood cells' cytoskeleton, arterial endothelium [7], and embryonic stem cells' nuclei [26]. Moreover, auxetics exhibit enhanced mechanical properties such as indentation resistance [27], fracture toughness [28], energy absorption [23,29], shear stiffness [30], and acoustic behavior. These properties make auxetic an excellent choice for various applications, ranging from sports [31] to biomedical applications [32–39].

The feasibility of auxetic structures applied to stent design has been studied in several studies. A study by Bhullar et al. [7] found that arterial endothelium has an NPR behavior when being subjected to both wall shearing and circumferential strain, causing axial compression (or tension) and transverse contraction (or expansion), which can decrease deformation incompatibility and promote tissue regeneration. An investigation of the mechanical properties of conventional anti-tri chiral stents was performed by Ruan et al. [40]. The researchers discovered that the mechanical properties of stents, such as the values of Poisson's ratio and Young's modulus, significantly depend on the core geometry. Wu et al. [41] used FEA to investigate the mechanical properties of the anti-tetra chiral auxetic stents, which showed significant radial expansion while maintaining their axial stability. Ren et al. developed metallic

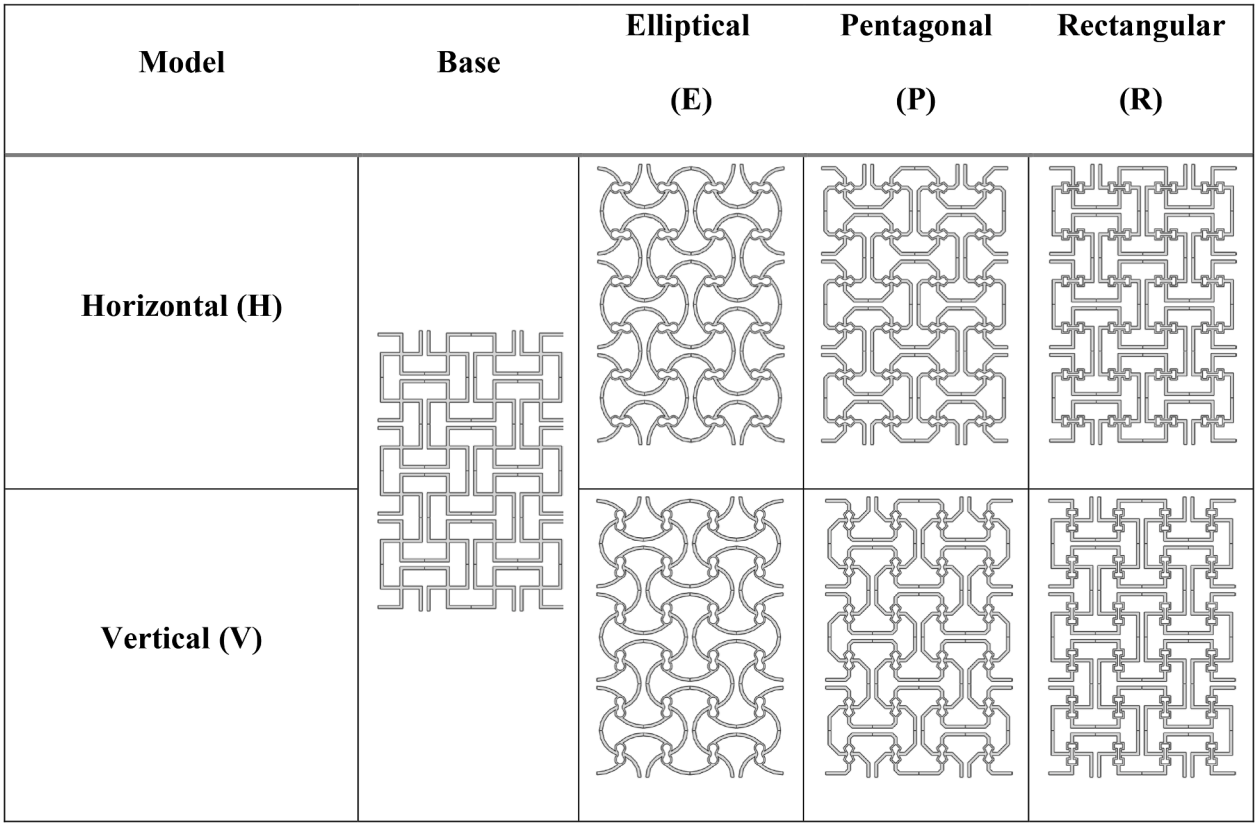

Fig. 4. 2D metamaterial designs.

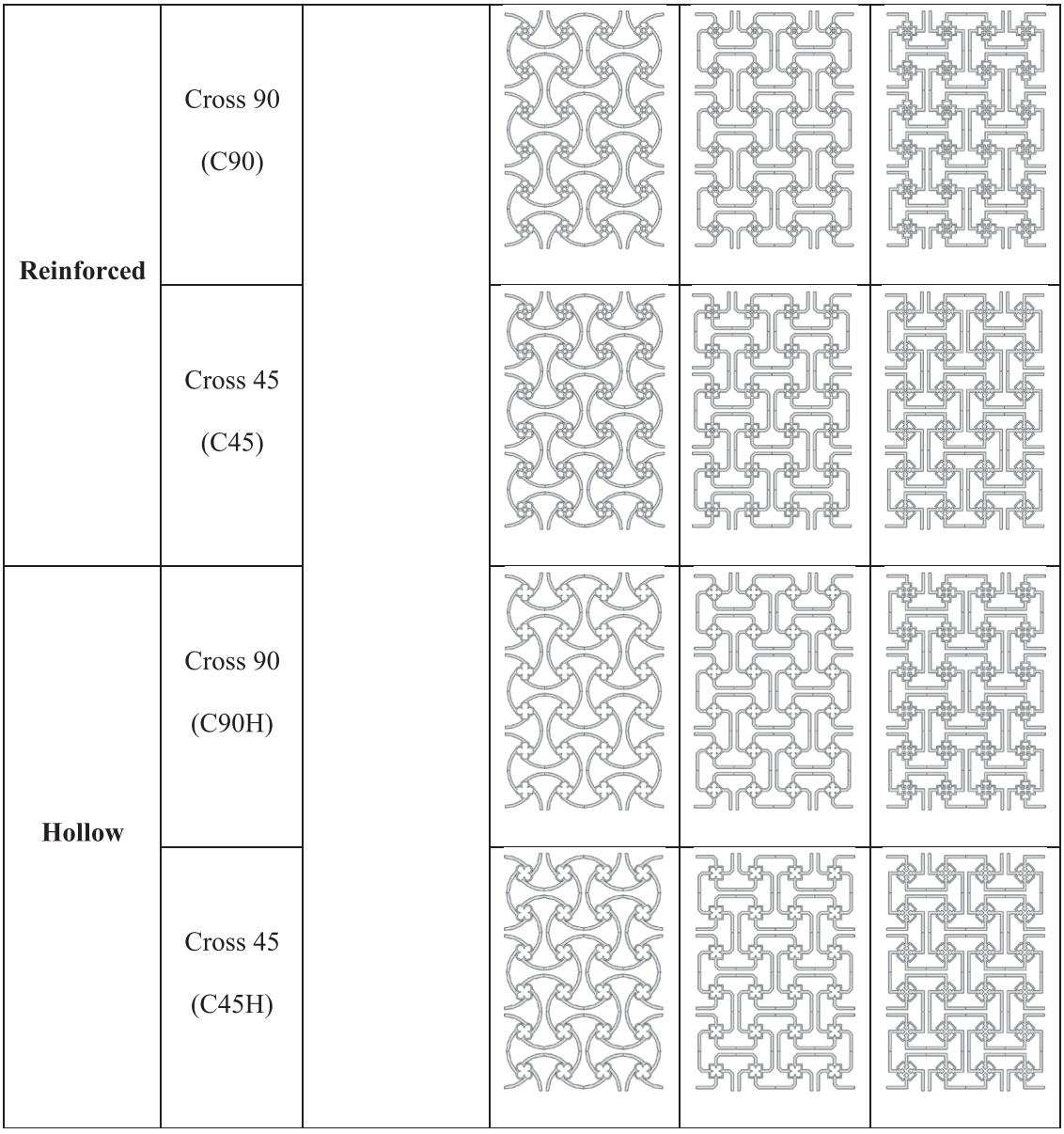

Fig. 4. (*continued*).

Table 3
Relative density of the presented cellular structures.

Model		Base	Elliptical (E)	Pentagonal (P)	Rectangular (R)
Horizontal (H)		0.24	0.195	0.219	0.256
Vertical (V)			0.195	0.219	0.256
Reinforced	Cross 90 (C90)		0.215	0.254	0.275
	Cross 45 (C45)		0.233	0.238	0.294
Hollow	Cross 90 (C90H)		0.191	0.221	0.268
	Cross 45 (C45H)		0.209	0.236	0.287

auxetic tubular structures based on the latest methodology for generating 3D auxetic metamaterials [42]. The tubular structure exhibited auxetic behavior in compression and tension, making it an excellent stent candidate. Geng et al. [5] described a chiral stent with two configurations. As a result, the chiral stent possessed a NPR under tensile loading. A Ni-rich TiNi auxetic origami stent graft was proposed by Kuribayashi et al. [43], which may be inserted at body temperature or by super elasticity deformation. The study by Gatt et al. also reviewed the feasibility of three types of hexagonal honeycombs arranged in three different designs: Non-reentrant, Re-entrant, and Hybrid honeycombs [44]. Simulated results indicated that non-re-entering stents might migrate, while hybrid stents might experience higher levels of inflammation due to their shorter supporting lengths. Hamzehei et al. [45] developed a 2D triangular anti-tri chiral geometry and cylindrical stent to achieve uniform shrinkage properties and high energy absorption under compression. According to the study, the triangular anti-tri chiral stent has a three times higher absorption capability than the conventional anti-tri chiral stent.

There are three categories of auxetic metamaterials based on their dominant deformation mode: re-entrant, rigid rotation, and chiral [46]. A chiral auxetic unit cell consists of a central node connected by several tangent ligaments. It has been shown that chiral lattices display superior out-of-plane properties and could therefore be used in flexible or energy-absorbing systems [47]. Like chiral, missing rib lattices (tri, anti-tri, tetra, anti-tetra, and Hexa-missing rib) were then proposed by

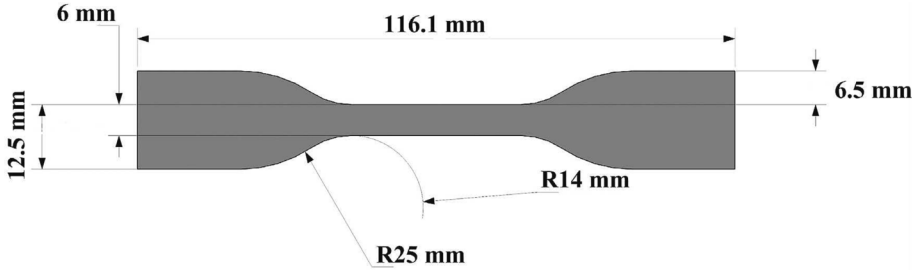

Fig. 5. Geometric dimensions of the standard uniaxial tensile test specimen.

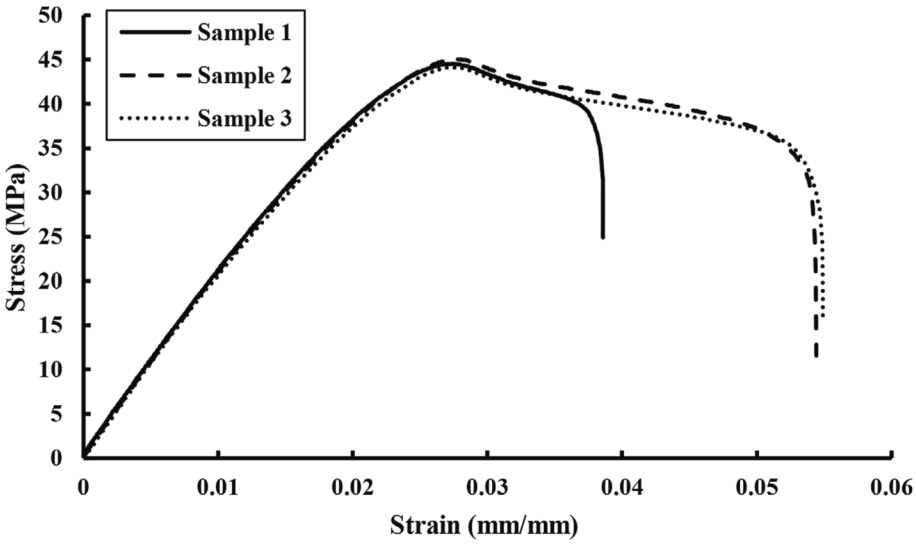

Fig. 6. The stress-strain curves of the tensile PLA specimens.

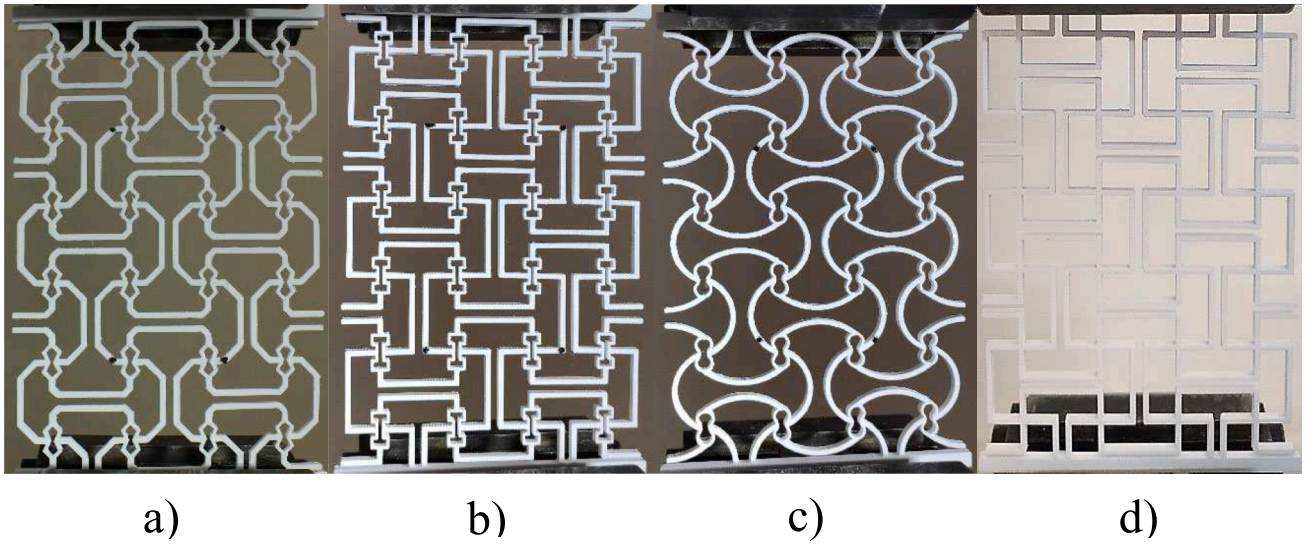

Fig. 7. Two-dimensional manufactures structures: (a) “P”, (b) “R”, (c) “E”, (d) “base”.

substituting a softer truss element for the rigid central node [47,48]. It results in a more stable Poisson’s ratio performance within a wide range of deformations compared to the chiral auxetics [49,50]. Various mechanical properties can also be tuned by using soft corner hinges in zigzag ligaments or reinforcing truss elements in the central region [51]. In addition to achieving tunable NPRs while improving stiffness, Zhu et al. also utilized simple straight beam reinforcement within the central trusses to investigate the properties of the improved Hexa-missing rib auxetic structure [49]. On the other hand, a chiral structure is usually subject to stiffness compromises to attain a tunable NPR. By combining three auxetic unit cells: re-entrant, trichiral, and anti-trichiral, Abbaslou et al. [52] developed a novel re-entrant *meta*-tri chiral auxetic (RMCA) vascular stent. An outstanding performance among auxetic structures was shown by the RMCA structure with an NPR of −4.91. Qi et al. [53]

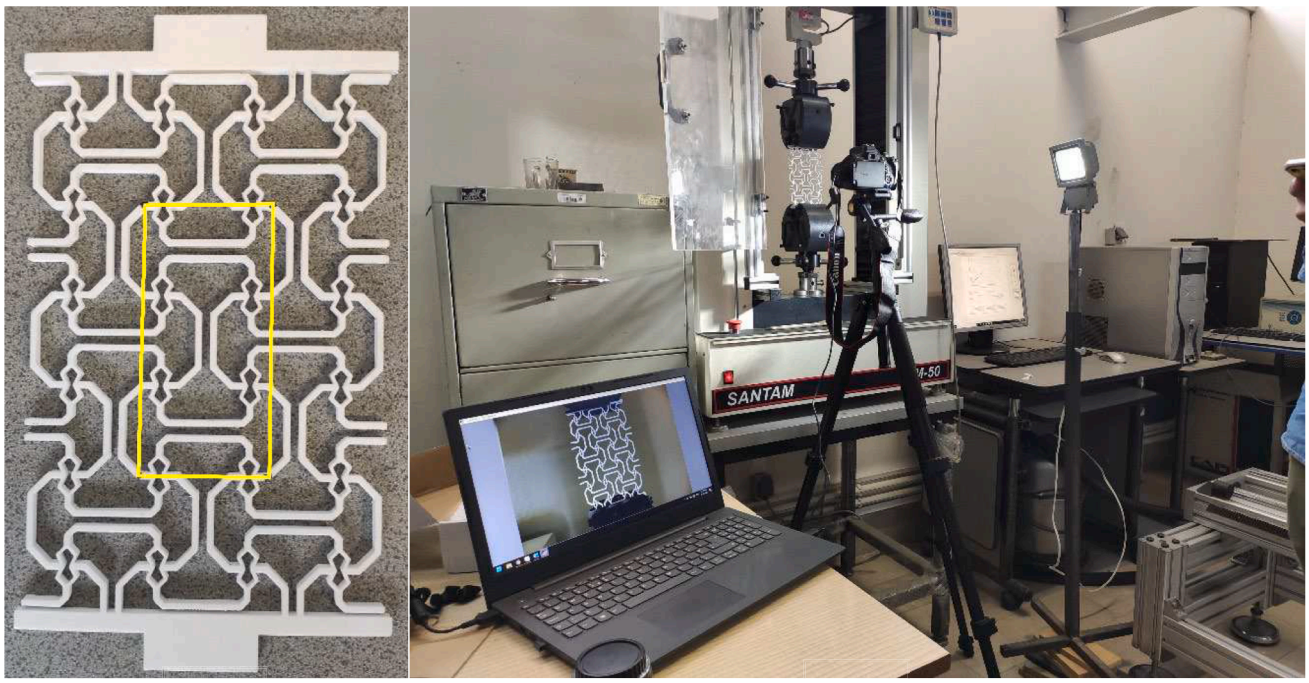

Fig. 8. (a) Marked Points on the sample to measure the Poisson's ratio, (b) Test setup.

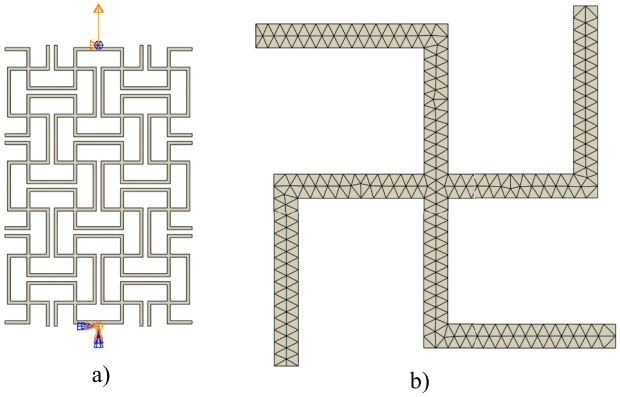

Fig. 9. 2D FE model: (a) Boundary conditions, (b) mesh.

introduce innovative 3D chiral metamaterials created by combining the deformation characteristics of re-entrant and antichiral unit cells. they explore the interplay of tension and rotation deformation mechanisms within these novel 3D chiral metamaterials using comprehensive large deformation theories. To validate theoretical models, they carry out both experimental and numerical investigations and further elucidate the deformation mechanism through parametric studies of the geometric properties.

Additive manufacturing, commonly known as 3D printing [54], represents a transformative technology in object creation. Among the various methods, Fused Deposition Modeling (FDM) emerges as a popular and accessible approach. FDM [55,56]functions by extruding thermoplastic filament layer by layer, gradually constructing the desired object. Its simplicity and cost-effectiveness position it as a preferred choice for rapid prototyping and small-scale production, providing versatility in materials and applications. Through FDM, intricate and customized designs attain newfound feasibility, heralding a new era of innovation and manufacturing potential.

Given the alarming mortality rate associated with arterial blockage, the exploration of intravascular stents is timely and vital today. Through precise geometric modifications of the missing rib unit cell, auxetic stents were ingeniously tailored to achieve unparalleled performance. The two main objectives of the works are as follows. The study encompasses the development and comprehensive analysis of eighteen meticulously crafted stents, with a primary focus on their biomedical efficacy.

- The transformative potential of missing rib unit cells in enhancing the biomechanical characteristics of medical stents, including load-bearing capacity, expanded opening percentage, and reduced recoil percentage.
- The mitigation of common drawbacks of medical stents such as foreshortening, and dog-boning.

Fig. 1 elucidates the step-by-step workflow employed in this investigation, encompassing the design of auxetic unit cells, experimental procedures, FEA, and an in-depth assessment of mechanical performance, including recoil percentage, dog-boning, and other related factors.

2. Methodology

2.1. Auxetic unit cell designs

Fig. 2 shows a development plan for designing the auxetic unit cells. Firstly, the cores with specific geometries are added to the "Base" unit cell by considering the missing ribs. By modifying the geometry of the core and the outer ligaments, three models of "Elliptical" (E), "Pentagonal" (P), and "Rectangular" (R) are developed. Then, the developed unit cells are considered in four different forms, including, "Vertical" (V), "Horizontal" (H), and "Crossed" with an angle of 90° and 45° to the horizon (C90, C45). Finally, h ollow (H) models are also considered to investigate the effect of inner ligaments.

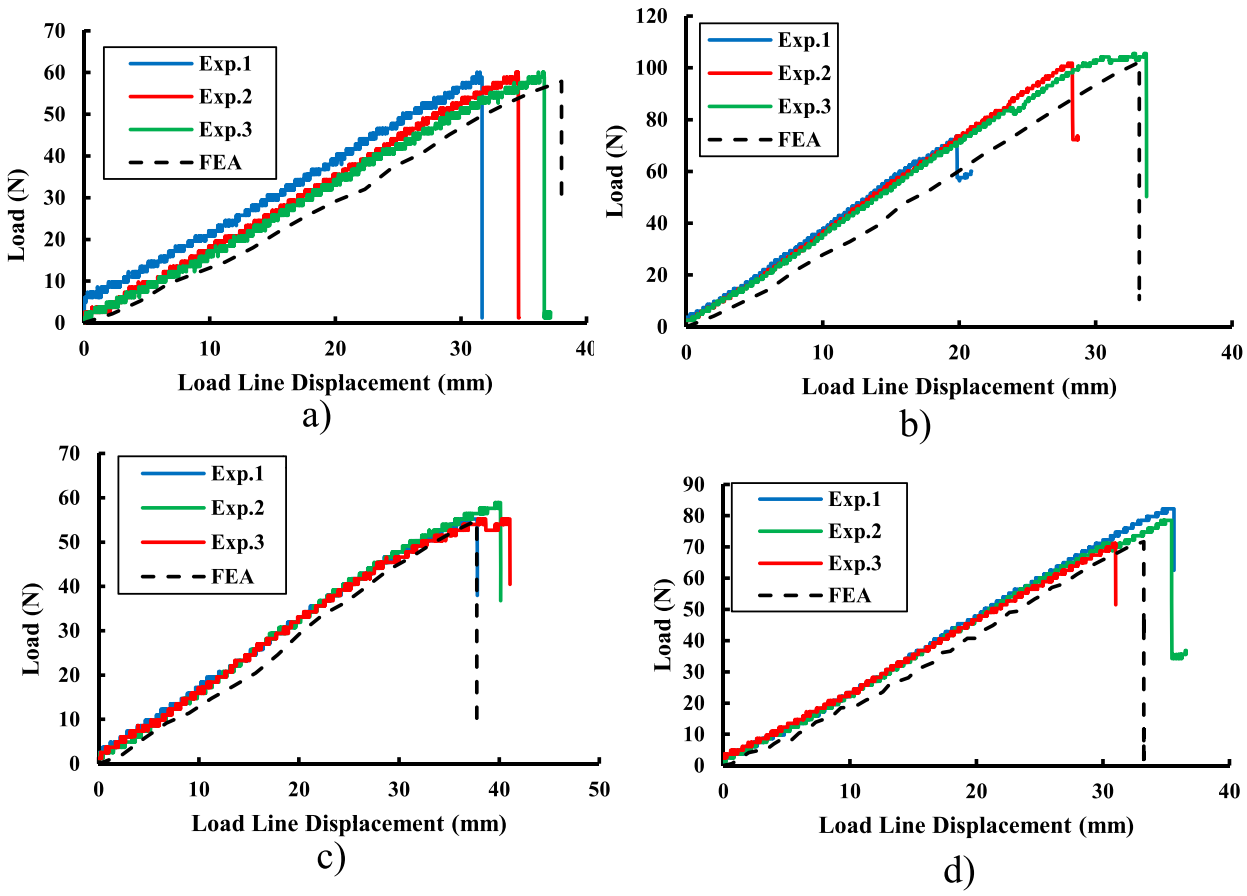

Fig. 10. Force-displacement relations of 2D lattice metamaterials (a) "Base",(b) "EV",() "PV",(d) "RV".

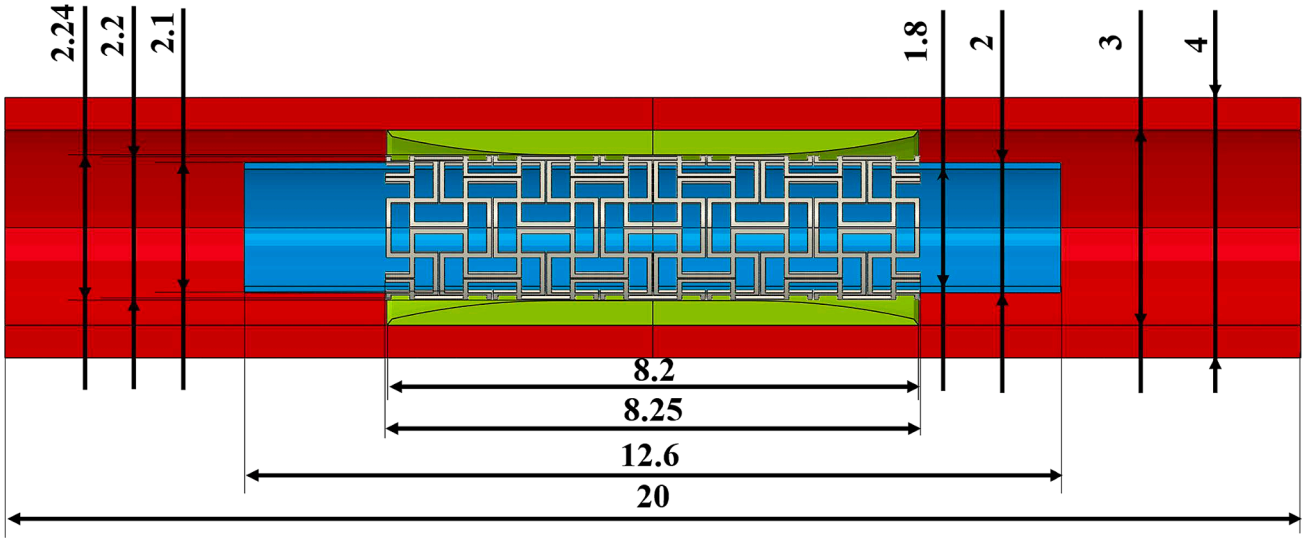

Fig. 11. Schematic of the balloon-stent-plate-artery system (unit: mm).

2.2. Structural design

Geometrical parameters related to the unit cells are shown in Fig. 3. Wall lengths 'H', 'L', and 'W', lengths 'a_1 : a_4' and thicknesses, 't_1' and 't_2' for the internal and external ligaments, respectively. An out-plane structure's thickness (depth) is indicated as 'B'. The constraint of geometric conditions must meet three criteria as follows. 1) $H > \frac{t_1}{2}, L > \frac{t_1}{2}$; these constraints must prevent core unit cells from self-contacting. 2) $a_1 + \frac{t_2}{2} > x_m, a_2 + \frac{t_2}{2} > y_m$; these constraints keep the core unit cell from contacting the external ribs, where 'x_m' and 'y_m' are the horizontal and vertical distances of point 'm' from the origin of the coordinate system respectively. 3) $a_3 > a_1 + \frac{t_2}{2}, a_4 > a_2 + \frac{t_2}{2}$; these constraints avoid contact between external ribs [57]. The information corresponding to the dimensions of the models are provided in Tables 1 and 2 for $t_2 = 1.6mm$.

To create 2D lattice metamaterials, unit cells shown in Fig. 3 are first mirrored relative to the end rib in each direction, then patterned by 2×3

Table 4
Coefficients of balloon-plaque-artery hyperelastic model [10].

	Arterial wall (kPa)	Plaque (kPa)	Balloon (kPa)
A_{10}	18.90	−495.96	1030
A_{01}	2.75	506.61	3690
A_{20}	85.72	1193.53	0
A_{11}	590.43	3637.80	0
A_{30}	0	4737.25	0
D_1	0	0	0

in both horizontal and vertical directions (Fig. 4). The nomenclature of the structures is according to the nomenclature of the unit cells presented in Fig. 4.

2.3. Relative density

The relative density is defined as the ratio of the density of the lattice structure,ρ^*, to the density of the material that the structure was made from, ρ_s. The relative density is one of the most important parameters of the auxetic structure behaviors and directly affects the structure's mechanical properties[57]. The relative density of the provided unit cells has been calculated using commercial software, SolidWorks, and presented in Table 3.

According to Table 3, the "E-category" structures have the lowest relative density, especially the "EC90H" unit cell. To compare the behavior of other presented unit cells, it is necessary to check each structure's behavior and mechanical properties such as Young's modulus and Poisson's ratio. To accomplish this, relevant experimental tests must be conducted, and numerical validations must be performed.

3. Exprimental study

3.1. Material properties

In this research, polylactic acid (PLA) was used to make two-dimensional samples presented in Fig. 5. The uniaxial tensile test according to ASTM standard D638-type IV [37], as shown in Fig. 5, was performed to evaluate the mechanical properties of PLA. Tensile tests were conducted at a constant speed of 1 mm/min using a SANTAM STM-50 testing machine with a 50 KN load cell, and the stress-strain responses are shown in Fig. 6.

3.2. Fabrication

The 2D structures shown in Fig. 4 were fabricated via fused deposition modelling (FDM). The dimensions of the structures were 144×96×3 mm, and the geometry of the unit cells follows Tables 1 and 2. Nozzle and bed temperatures were set at 210 and 60 °C, while nozzle diameter and speed were set at 0.4 mm and 50 mm/s, respectively. A generous production budget and time allowed only the "Base", "EV", "PV", and "RV" structures to be manufactured and tested (Fig. 7).

3.3. Tensile test

The tensile test of the 2D samples shown in Fig. 7 was performed using SANTAM STM-50 testing machine with a 5 mm/min loading rate. The deformation mechanisms were recorded by optical camera photography (Fig. 8(a)). In addition, to calculate Poisson's ratio of each 2D sample, the displacements of specific points far enough from the boundaries were measured (Fig. 8(b)).

4. Numerical validation

4.1. Numerical simulation of 2D metamaterials

ABAQUS/explicit commercial software was adopted to model the 2D structures according to the general dimensions (144 × 96 × 3) and unit-cells local dimensions provided in Tables 1 and 2. From Fig. 6, it is seen that the PLA shows elastic-plastic behavior. Thus, elastic-plastic behavior with ductile damage definition was considered. A reference point was considered at each end of the model. The lower reference point was restricted entirely from all degrees of freedom for applying the boundary conditions, and the displacement load was applied to the upper reference point (Fig. 9(a)). As shown in Fig. 9(b), due to structural complexity, CPS3 triangular linear elements with a total seed size of 0.8 mm, 8640 elements for the model with the lowest relative density ("EC90H"), and 12,240 elements for the model with the highest relative density ("RC90") were considered to mesh the models.

4.2. FEA validation of 2D metamaterials

The force-displacement responses from the tensile tests of "Base", "EV", "PV", and "RV" lattice structures were shown in Fig. 10(a – d) respectively. Excellent coincidence can be seen in Fig. 10, where the

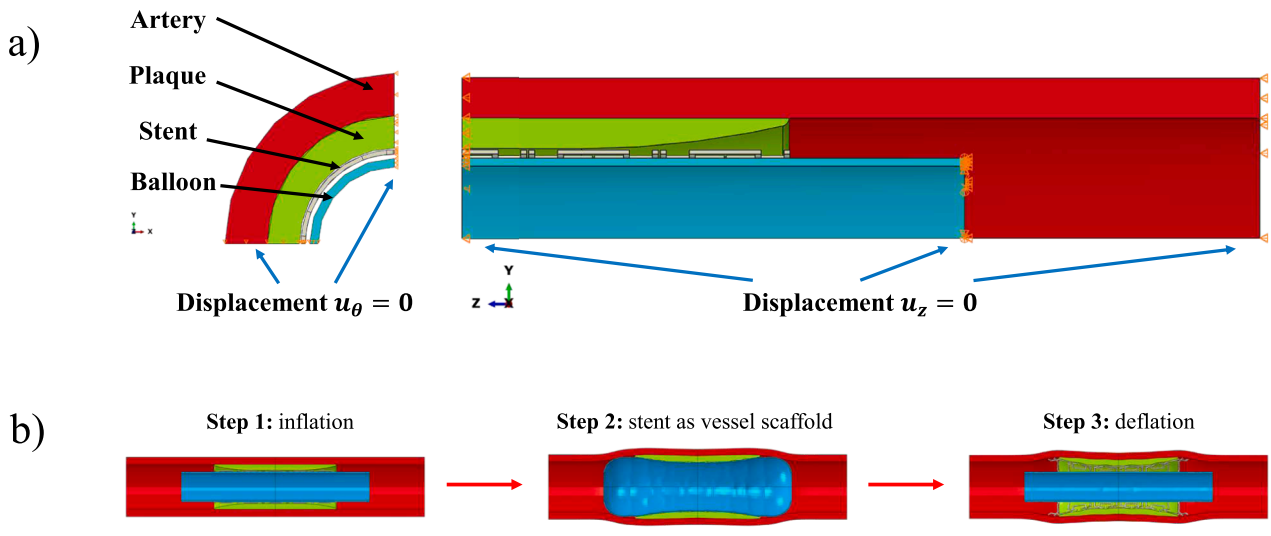

Fig. 12. (a) Boundary conditions of balloon-stent-plaque-artery system, (b) schematic of the stent insertion process in the artery.

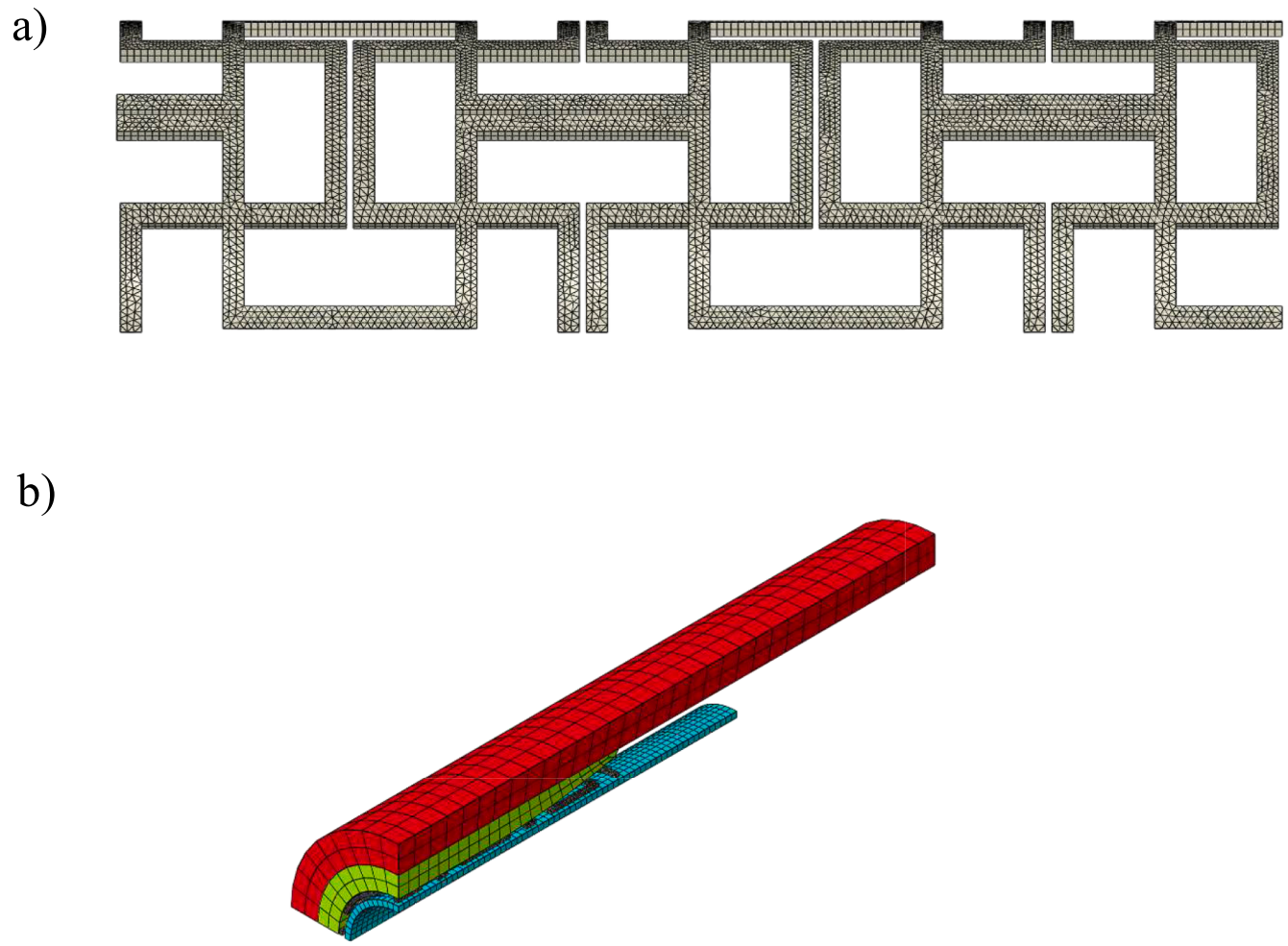

Fig. 13. (a) Stent mesh, (b) mesh of the system parts.

numerical and experimental force-displacement curves show a reasonable accuracy (5–15 % engineering error). Due to the brittleness of the parent material, PLA, lattice metamaterials show linear elastic behavior until fracture.

4.3. Numerical simulation of biomedical stents

Finite element models of the missing rib structure, including all the structures presented in Fig. 4, were modelled with the ABAQUS\e xplicit FEA. Due to the biaxial symmetry of the model, a balloon-stent-plaque-artery system has been modelled as a quarter of the full system. Plaque tissue varies from a zero-stenosis ratio at the end of the plaque to a 45 % stenosis ratio in the middle. The schematics and geometry of the vessel, plaque, and stent were presented in Fig. 11 [58]. The primary system is such that the stent is properly assembled on the balloon, and the opening process starts inside the plaque by respecting the distance from the inner surfaces of the vessel.

Due to the appropriate biomechanical behavior, such as excellent compatibility with the body environment and proper expansion, SS316L stainless steel has been used as a stent material. The elastic properties were considered, density $\rho = 7800\frac{kg}{m^3}$, Young's modulus $E = 196GPa$, and Poisson's ratio $\nu = 0.3$ [58]. To define the behavior of balloon, plaque, and artery, the constitutive hyperelastic model with the third-order strain energy density function of Eq. (4) was used [10].

$$W = A_{10}(I_1-3) + A_{01}(I_2-3) + A_{20}(I_1-3)^2 + A_{11}(I_1-3)(I_2-3) + A_{30}(I_1-3)^3 + \frac{1}{D_1}(J-3) \tag{4}$$

where the coefficients A_{ij} and D are the hyperelastic model parameters, I_1, I_2 and J are the first, second and third stretch invariants respectively. The density of all three materials of the balloon, plaque, and artery was considered equal, $\rho = 1070\frac{kg}{m^3}$ and the A_{ij} coefficients for each material are presented separately in Table.4.

The interactions between different system members were defined as general surface-to-surface contact with a friction coefficient of 0.1. The contact surfaces between plaque and artery were tied to each other. To prevent rigid body motion of the stent during the inflation and deflation stages, the translational degree of freedom in the longitudinal direction of the artery at the symmetry line of the system and the ends of the artery were restricted. Also, to establish symmetry conditions, the angular displacement was restricted to the angular sides of the model (Fig. 12 (a)).

The stent placement process can be broken down into three main stages, depicted schematically in Fig. 12(b). The first step involves balloon expansion. This causes the stent to change shape and extend, allowing it to contact the plaque. In the second stage, the expansion of the balloon continues, providing support to the stent against resistance from the artery and the plaque. This support is crucial until the stent is

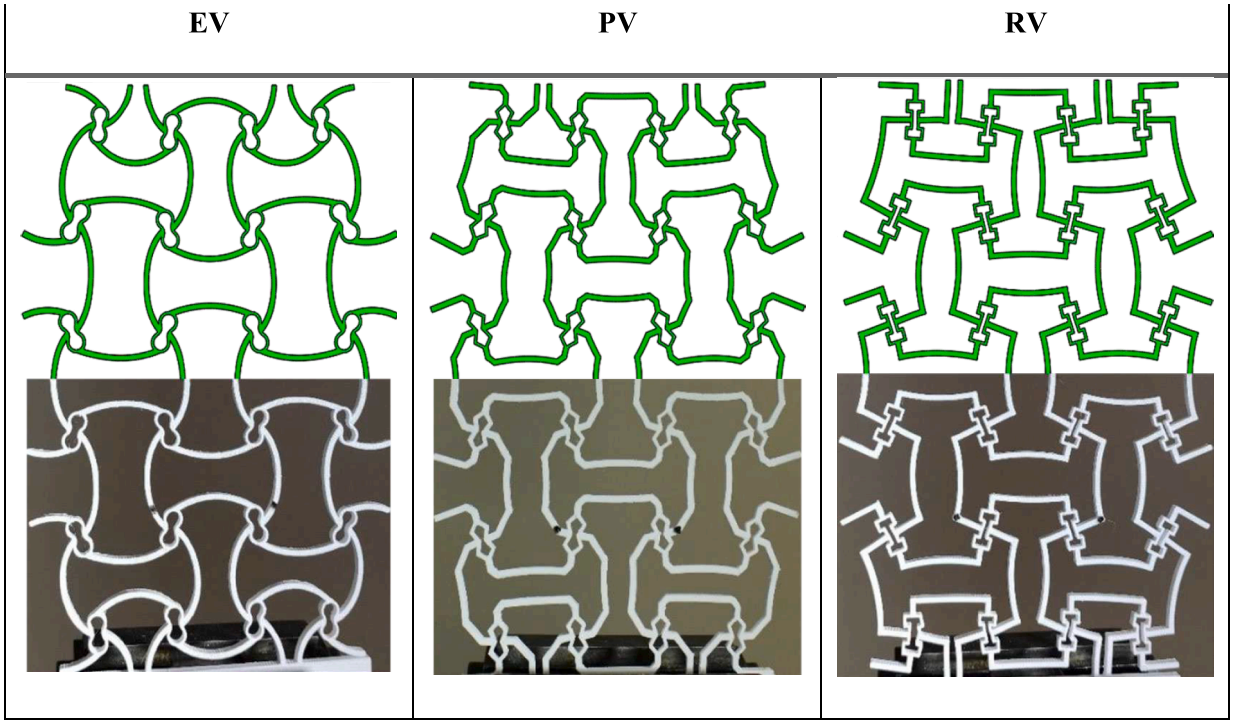

Fig. 14. Comparison of numerical and experimental analyses of deformation mechanisms.

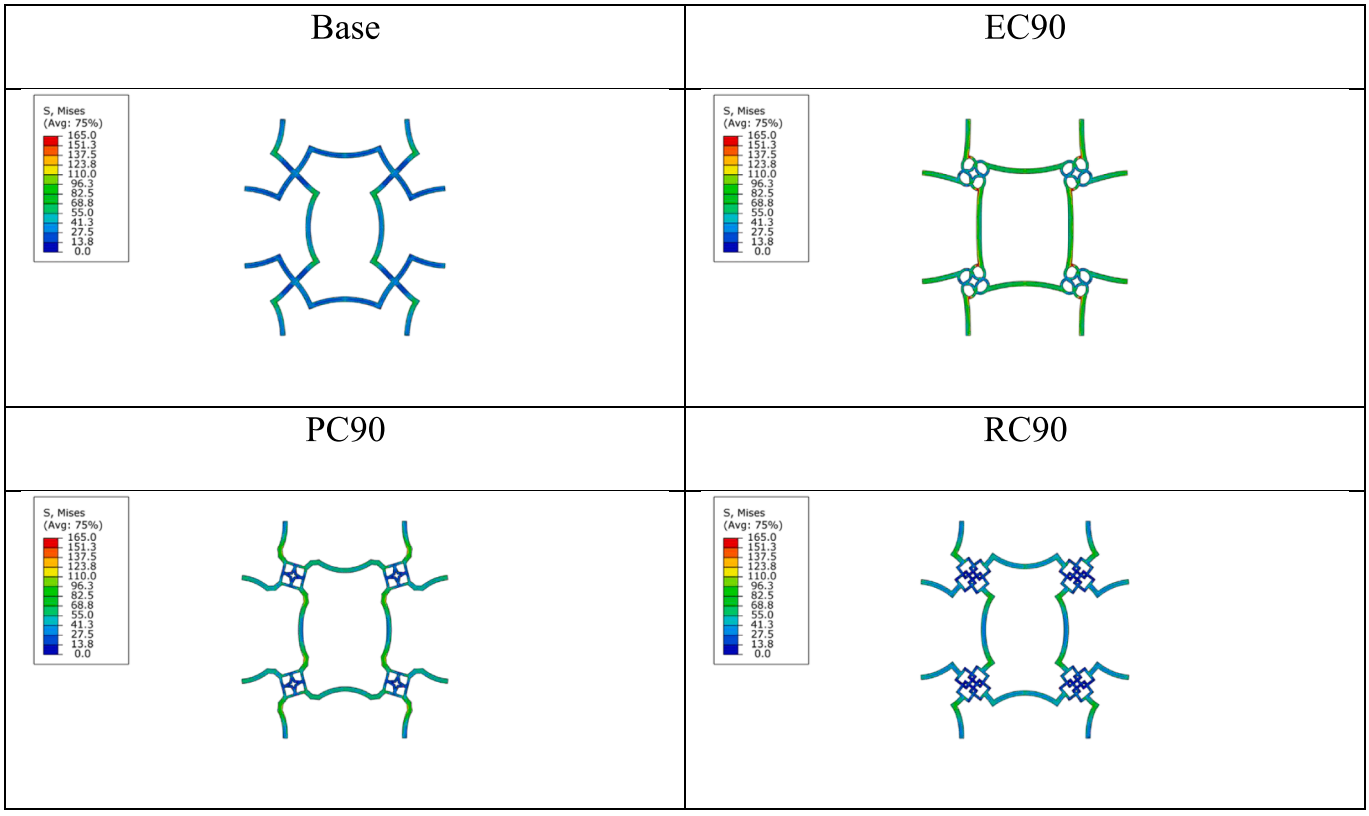

Fig. 15. Von Mises stress field in some of the presented structures.

fully opened and sufficient plastic deformation occurs within it. Finally, in the third stage, the balloon is deflated. However, the residual plastic deformation in the stent acts as a scaffold within the vessel. This leads to the opening of the artery, restoring proper blood flow. By following these steps, stent placement helps to alleviate blockages in the arteries and restore healthy circulation.

Due to the chiral structural complexity, C3D6 mesh with a total seed size of 0.025 mm (two element rows along the thickness) was utilized to

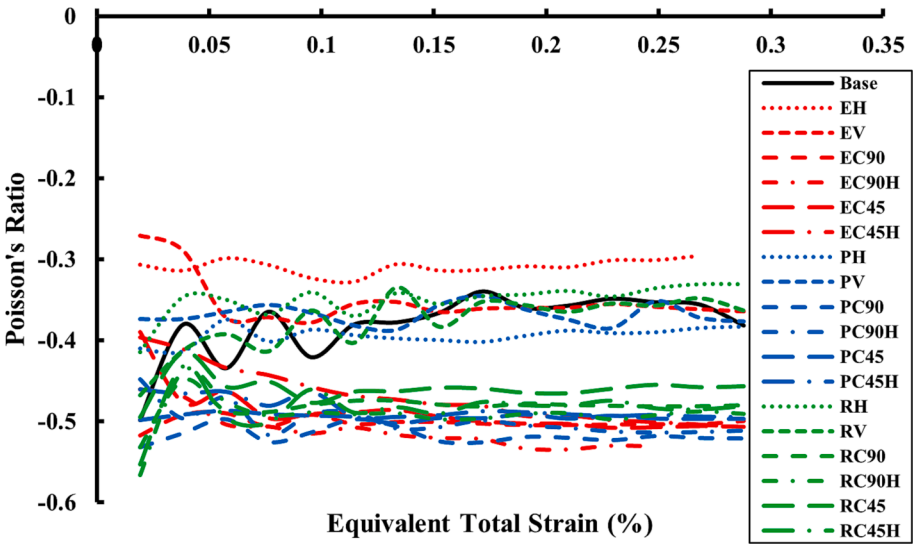

Fig. 16. Numerical Poisson's ratio versus equivalent total strain curves for different unit cells.

Table 5
Experimental and numerical Poison's ratio of "Base", "EV", "PV", and "RV" structures.

Analysis	Unit Cell			
	Base	RV	PV	EV
Experimental	−0.411	−0.403	−0.391	**−0.364**
FEA	−0.381	−0.377	−0.364	**−0.351**

mesh the stent as shown in Fig. 13(a). Moreover, due to the hyperelastic behavior of the balloon, plaque, and artery, the C3D8I elements were used to mesh members (Fig. 13(b)).

5. Results & discussion

5.1. Deformation mechanisms of 2D metamaterials

Fig. 14 illustrates the deformation mechanisms of 2D structures subjected to tensile forces, as investigated through both numerical simulations and experimental techniques. Initially, during the onset of loading, the external ligaments of the unit cells start to open due to distinct rotations within their cores. This initial deformation leads to the primary auxetic behavior of the structure becoming evident. As the loading progresses, the external ligaments continue to open until they reach their maximum limit, at which point the core of the cells also begins to open. This secondary deformation results in a secondary auxetic behavior. In all these structures, a significant negative Poisson's ratio (NPR) is observed, which arises from the combined effects of both primary and secondary auxetic behaviors.

Fig. 15 shows the Von Mises stress distribution within several presented structures, denoted as "Base," "EC90," "PC90," and "RC90." The visual representation in Fig. 15 underscores that a significant proportion of the structural load is borne by the ligaments connecting the cores. This observation raises concerns regarding structures lacking curvature, as they tend to generate multiple stress concentration points, consequently diminishing their load-bearing capacity. Furthermore, it is noteworthy that, within each structural category, crossed configurations consistently exhibit superior load-bearing capabilities. Previous research has demonstrated that augmenting the core's stiffness through the introduction of new ligaments aligned with the loading direction can enhance the overall structural stiffness [60], as exemplified by the force-displacement curves depicted in Fig. 10. This phenomenon elucidates the heightened load-bearing capacity observed in crossed structures.

Fig. 16 shows the Poisson's ratio of different structures versus the equivalent total strain in the loading direction. The equivalent total strain can be written as $\epsilon = \frac{\Delta L}{L}$ where L is the initial length of the model and ΔL is the change in the initial length during loading. Moreover, Table 5 shows the average values of Poisson's ratio measured by experimental tests. Structure development resulted in a moderate increase in auxeticity compared to the "Base" model, as shown in Fig. 16. In addition, the curved ligaments of the structures reduce resistance during the opening process, resulting in a significant increase in auxetic behavior. Thus, "E-category" structures, especially "EC90H" structure, shows the highest NPR. Moreover, "P-category" structures show the second highest Poisson's ratio. The key observation pertains to the manifestation of negative Poisson's ratio (NPR) behavior in the pure horizontal and vertical models. Remarkably, the Poisson's ratio values in these models closely resemble that of the base model. Consequently, the utilization of combined vertical and horizontal models emerges as a more suitable approach for achieving higher NPR behavior. The simultaneous existence of horizontal and vertical joints contributes to increased stiffness within the joints, facilitating smoother and more effortless bending of the surrounding walls. This phenomenon results in a heightened NPR response under mechanical loads, showcasing enhanced deformation characteristics.

5.2. Deformation mechanisms of biomedical stents

Fig. 17(a and b) display the deformation patterns of the stents labelled as "Base," "PC90," "EC90," and "RC90." Additionally, Fig. 17(b) provides the radial displacement-balloon pressure curves for all these distinct models. All three categories share identical deformation mechanisms, yet the specifics of these mechanisms differ depending on the unit cell type. As depicted in Fig. 17(b), the stent model "Base" exhibits the greatest maximum radial expansion. However, this expansion is not sustained within the stent during the balloon deflation phase and reverts to its original state, reaching approximately 55 % of the maximum expansion. Apart from the "Base" model, the stents within the "R" and "P-category" exhibit the highest maximum expansion, with roughly similar average radial displacement values. In contrast, the "E-category" models display the lowest degree of expansion. Across all three categories, the stent models labelled as "vertical" (V) and "Crossed" (C90) exhibit the most extensive maximum expansion, while the "horizontal" (H) models display the least maximum expansion. This maximum expansion highlights the pronounced auxetic behavior of these models.

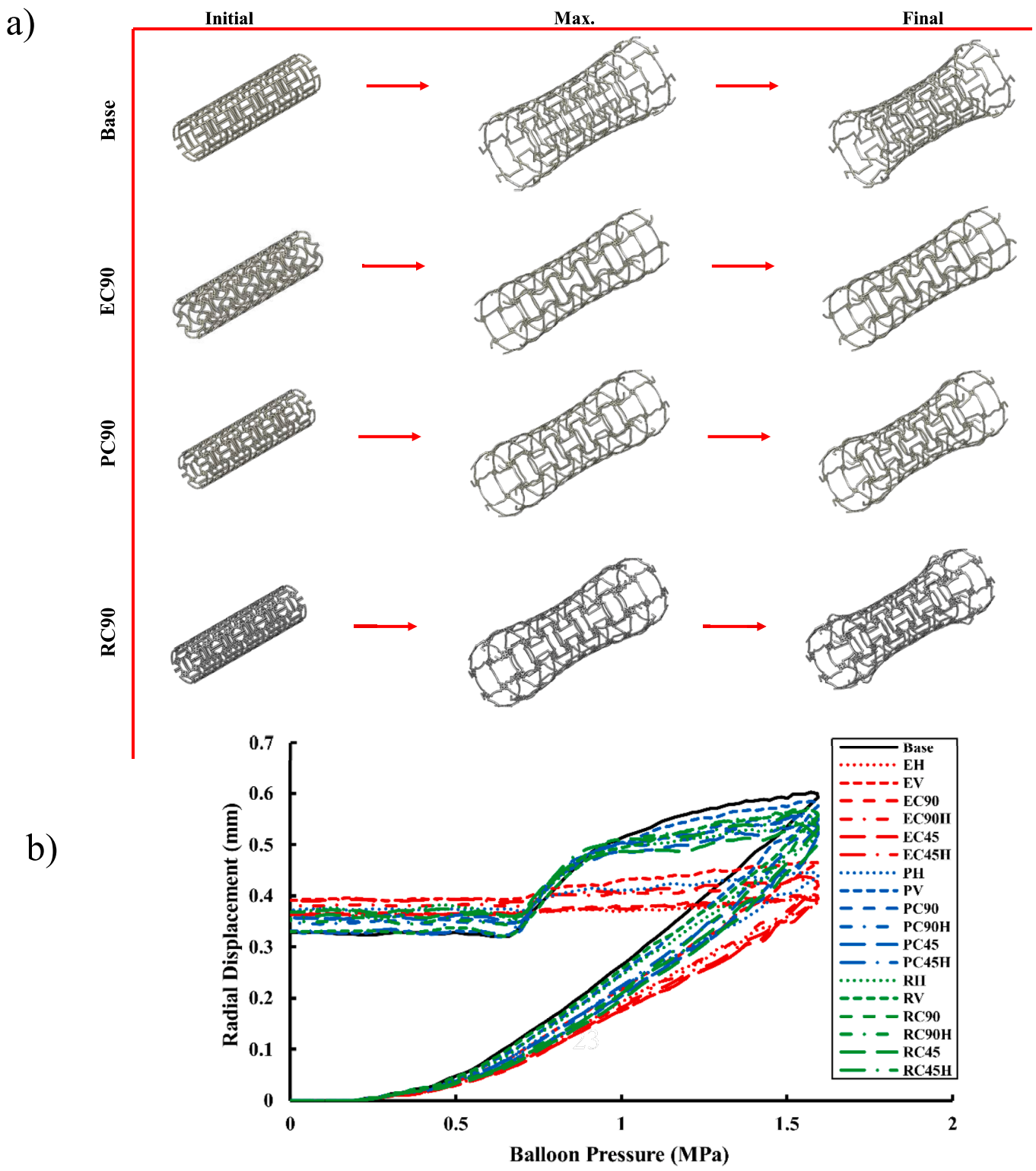

Fig. 17. (a) Deformation mechanisms in "Base", "EC90", "PC90", and "RC90" models, (b) the radial displacement-balloon pressure curves for presented models.

Nevertheless, in medical applications, the most critical parameter is the ultimate expansion achieved after the deflation phase. Upon inspecting the final expansion values in Fig. 17(b), it becomes apparent that the behavior of radial displacement contrasts with that of maximum expansion. Specifically, the "E-category" models demonstrate the highest final expansion in this regard.

5.3. Recoil and dog-boning

During the stent placement process, non-uniform deformations in the stents can lead to severe damage to the arterial tissue. To examine the effect of uniform and non-uniform deformations, the final opening can be defined as a percentage of the maximum opening, so-called recoil parameter, in the form of Eq. (5) [10,58].

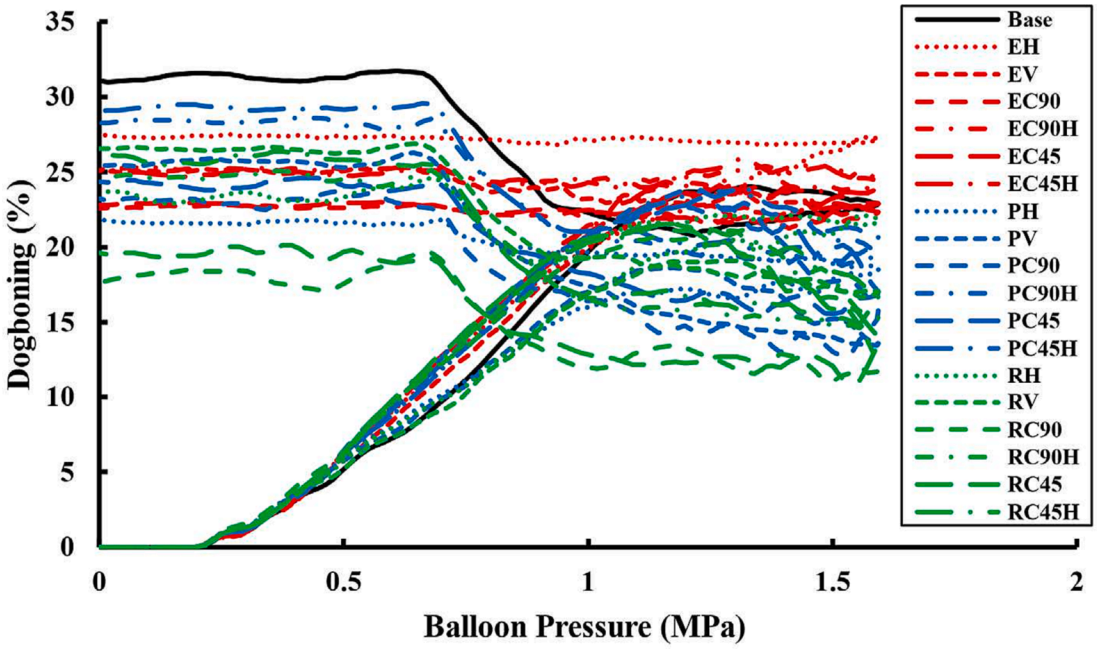

Fig. 18. Dog-boning percentage versus balloon pressure curves of the studied models.

Table 6
Recoil percentage of the stents.

Model		Base (%)	E (%)	P (%)	R (%)
Horizontal		15.567	1.710	4.288	9.523
Vertical			4.508	14.641	13.435
Reinforced	Cross 90		1.923	9.907	10.399
	Cross 45		1.628	10.070	8.318
Hollow	Cross 90		2.541	12.110	12.377
	Cross 45		1.841	12.389	10.736

Table 7
Dog-boning percentage of the stents at the end of deflation step.

Model		Base (%)	E (%)	P (%)	R (%)
Horizontal		31.062	27.440	21.813	23.746
Vertical			25.084	25.416	26.561
Reinforced	Cross 90		22.588	23.218	17.647
	Cross 45		22.789	24.339	19.611
Hollow	Cross 90		25.196	28.241	24.626
	Cross 45		25.126	29.060	26.174

$$Recoil = \frac{r_{mid,max} - r_{mid,final}}{r_{mid,max}} \times 100 \quad (5)$$

where $r_{mid,final}$ is the radius of the stent in the middle after deflating and $r_{mid,max}$ is the radius of the stent in the middle at the maximum radial opening. The lower the value of the Recoil parameter, the more uniform the deformations of the stent during the opening and closing of the vessel during the insertion process, resulting in decreasing the probable damages to the arterial tissue. Non-uniform deformations caused by the elastic deformation release of the stent and the compression of the vessel tissue after the balloon deflation lead to the dog-boning phenomenon in the stents, where the central areas of the stent that are in contact with the plaque undergoes more deformation release compared to the ends. Dog-boning can cause significant damage to the peripheral region of the vessel around the plaque. The Dog-boning parameter can be defined as Eq. (6) [10,58].

$$Dogboning = \frac{r_{ends,final} - r_{mid,final}}{r_{ends,final}} \times 100 \quad (6)$$

where, $r_{ends,final}$ is the radius of the stent at the ends after balloon deflation. The dog-boning percentage-ballon pressure curves and the recoil percentage of studied models are presented in Fig. 18, and Table 6 respectively. The dog-boning percentages at the end of the insertion process are also provided in Table 7.

As indicated in Table 6, all the modified stents exhibit a reduced recoil percentage, with the "E-category" models displaying the lowest recoil values. Notably, the "horizontal" (H) models also rank among the stents with the lowest recoil percentages across all categories. The reduction of sharp points and the incorporation of curved ligaments within the stent design prove effective in mitigating recoil percentages. Conversely, the stents with the highest recoil percentages are the "PV," "RV," and "PC45H" models. It appears that positioning the core of the unit cell in the longitudinal direction of the stent results in a significant increase in stent expansion, albeit at the cost of higher recoil percentages during the final stages of stent placement. Among the stent models, the "E-category" models demonstrate the most extensive final expansion percentage. As illustrated in Fig. 18, the stents with the highest "dog-boning" effect are the "Base," "PC45H," and "PC90H" models. In contrast, the "R-category" models exhibit the lowest percentage of dog-boning, with the "RC90″ model recording the lowest value at 17.64 %.

Fig. 19 depicts the stress distribution within the stents labelled as "EC90," "PC90," and "RC90″ under the maximum balloon pressure. The presence of enhanced curved ligaments and cores in these models results in an uneven stress distribution and an overall decrease in stress levels within the stent. Consequently, when subjected to the same balloon pressure, these mentioned models exhibit greater resistance to expansion compared to models with curved ligaments and cores. This resistance diminishes the maximum displacement of the stent and its recoil. Conversely, the arterial tissue exhibits slight resistance to the expansion of stents with curved ligaments and cores, leading to lower stress levels and plastic strain in the areas surrounding the plaque. This ease of expansion causes a noticeable difference in deformation between the inner and outer regions of the plaque. As a result, the percentage of the "dog-boning" effect, where the stent has a tapered appearance, increases.

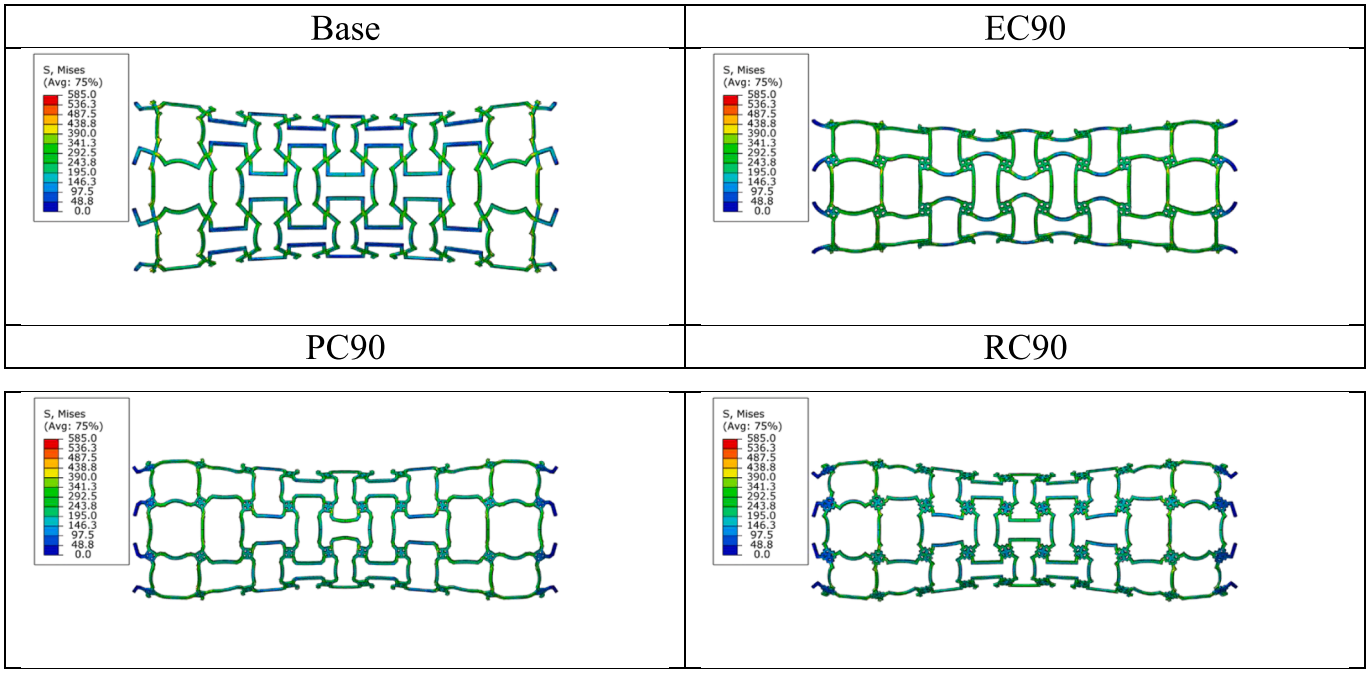

Fig. 19. Von Mises stress field in the "Base", "EC90", "PC90", and "RC90" models at the maximum balloon pressure.

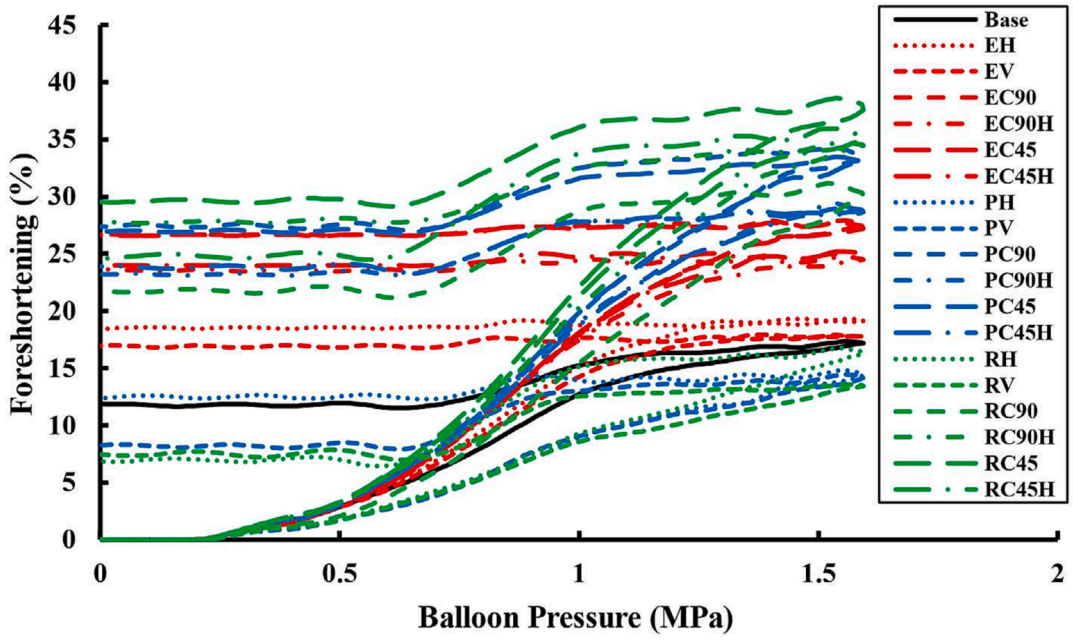

Fig. 20. Foreshortening versus balloon pressure curves for studied models.

Table 8
Foreshortening percentage of the stents at the end of deflation step.

Model		Base (%)	E (%)	P (%)	R (%)
Horizontal		11.843	18.457	12.366	6.832
Vertical			16.927	8.232	7.455
Reinforced	Cross 90		26.687	27.355	21.767
	Cross 45		26.640	26.934	29.531
Hollow	Cross 90		23.584	23.184	27.793
	Cross 45		23.969	23.899	24.605

5.4. Foreshortening

In the standard stents employed during the process of opening arteries, they exhibit a positive Poisson's behavior, which means that their length decreases after being deployed within the artery, depending on their structure. This reduction in length along the longitudinal axis is commonly referred to as "foreshortening." Foreshortening can potentially harm the arterial tissue and reduce effectiveness as it might not fully cover the plaque within the artery. Consequently, healthcare professionals and designers typically estimate the stent length to be slightly longer than its actual value to compensate for this effect. Conversely, in stents with a negative Poisson's ratio (NPR) behavior, foreshortening is

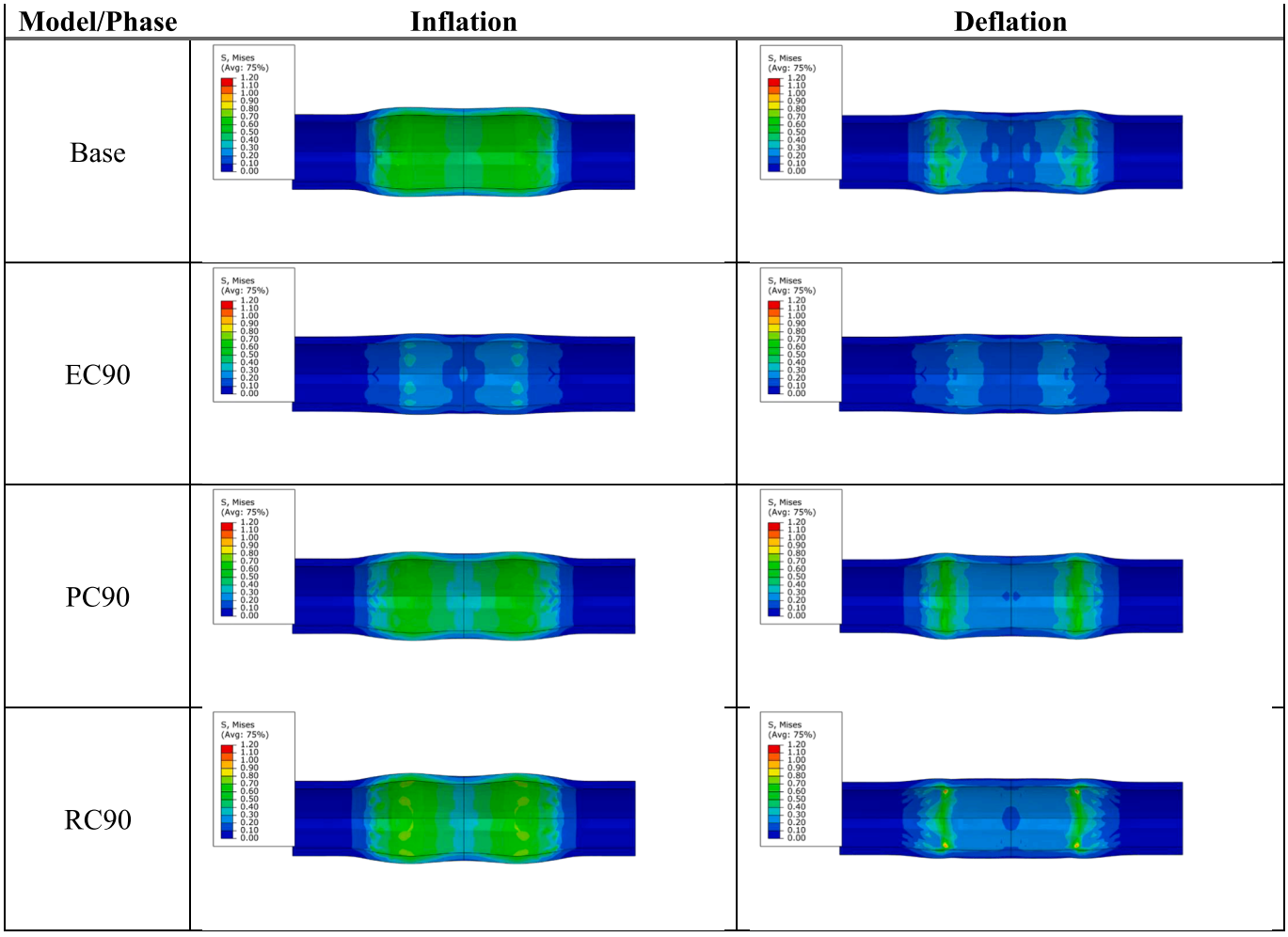

Fig. 21. Von Mises stress field of the artery due to "Base", "EC90", "PC90" and "RC90" models insertion.

less of a concern, as these stents actually elongate upon deployment. However, the increase in stent length, especially within curved arteries, can cause significant damage to the arterial tissue. Therefore, it's crucial to manage the foreshortening parameter within an appropriate range. This parameter is formally defined as Eq. (7) [59].

$$Foreshortening = \frac{L_{final} - L_{initial}}{L_{initial}} \times 100 \tag{7}$$

where $L_{initial}$ is the initial length and L_{final} is the final length of the stent during the stent placement process. Fig. 20 and Table.8 show the foreshortening percentage of the proposed models with different balloon pressure. As shown in Fig. 20, in all categories, the "horizontal" and "vertical" models (H, V) next to the "Base" model shows the lowest foreshortening percentage. The percentage of foreshortening in "PV", "RV", and "RH" models is less than 10 %, and the highest percentage of foreshortening also belongs to the "RC45" model. Moreover, changing the angle of the unit cell core from 90° to 45° leads to an increase in foreshortening, and hollowing the unit cell leads to a decrease. It is worth mentioning that there is no significant relationship between foreshortening and the Poisson's ratio of the 3D structure.

5.5. Intra-arterial stress field assessment

Fig. 21 illustrates the stress distribution within the artery resulting from the insertion of different stent types: "Base," "EC90," "PC90," and "RC90." As depicted in Fig. 21, the "EC90″ variant exhibits a consistent stress distribution because of its smooth contours, displaying lower stress levels both under pressure and after deflation when compared to the other stent models. Conversely, the "RC90″ model, characterized by its sharp edges, exhibits stress concentration at specific points within the arterial tissue. These points are precisely located at the end of the plaque tissue, where the dog-boning phenomenon is most noticeable. By addressing the issue of sharp edges and introducing the "PC90″ model, the stress concentration points disappear, and overall stress levels decrease. It's worth noting that while elevated stress levels with a uniform distribution typically do not result in significant damage to arterial tissue, stress concentration points in metallic stents can pose a risk during stent placement, potentially harming the artery. Therefore, extensive clinical investigation is necessary when selecting stents other than those falling under the "E-category" models.

6. Conclusion

This research provides invaluable insights into the customization of metamaterial stents for biomedical applications. These findings hold great promise for advancing the development of stent technology, ultimately leading to improved patient outcomes in the treatment of conditions such as arterial stenosis. In addition, this study delved deep into the mechanical behaviors and deformation mechanisms of 3D printed missing rib-based metamaterials, with a specific focus on their application in biomedical stents, particularly 2D lattice structures. Through intricate geometric modifications and rigorous analysis, several crucial findings have emerged:

- The modification of rib-unit cells, as exemplified by the "E-category" stent, demonstrated a remarkable reduction in recoil percentage compared to the base stent. While the base stent exhibited a significant recoil percentage of 15.56 %, the modified "E-category" stent showcased an impressive recoil percentage of only 1.62865 %. This underscores the pivotal role of geometric adjustments in minimizing recoil, a critical factor in stent performance.
- Increasing the curvature of ligaments and the core not only mitigated recoil but also achieved a more uniform stress distribution within the stent structure. Rounded edges and the incorporation of crossed designs, exemplified by the "EC90″ model, exhibited the highest load-bearing capacity. These refinements are vital in ensuring stent durability and its ability to maintain uniform stress on arteries, contributing to overall effectiveness.
- "E-category" stents stood out as the optimal choice among the studied models. These stents demonstrated the highest final opening capacity and the lowest recoil percentage, which are instrumental in minimizing arterial tissue damage while effectively treating arterial stenosis. Furthermore, core angle adjustments showed that the "E-category" stents were particularly well-suited for addressing foreshortening issues associated with arterial stenosis treatment.

Declaration of Competing Interest

The authors declare that they have no known competing financial interests or personal relationships that could have appeared to influence the work reported in this paper.

Data availability

Data will be made available on request.

Acknowledgments

This work is based upon research funded by Iran National Science Foundation (INSF) under project No. 4013397.

References

[1] J.A. van Diepen, J.F.P. Berbée, L.M. Havekes, P.C.N. Rensen, Interactions between inflammation and lipid metabolism: relevance for efficacy of anti-inflammatory drugs in the treatment of atherosclerosis, Atherosclerosis 228 (2) (2013) 306–315.
[2] D. Stoeckel, C. Bonsignore, S. Duda, A survey of stent designs, Minimally Invasive Therapy & Allied Technologies 11 (4) (2002) 137–147.
[3] J. Raamachandran, K. Jayavenkateshwaran, Modeling of stents exhibiting negative Poisson's ratio effect, Comput Methods Biomech Biomed Engin 10 (4) (2007) 245–255.
[4] V.H. Carneiro, H. Puga, Deformation behaviour of self-expanding magnesium stents based on auxetic chiral lattices, Ciência & Tecnologia Dos Materiais 28 (1) (2016) 14–18.
[5] L.C. Geng, X.L. Ruan, W.W. Wu, R. Xia, D.N. Fang, Mechanical properties of selective laser sintering (SLS) additive manufactured chiral Auxetic cylindrical stent, Exp Mech 59 (6) (2019) 913–925.
[6] Z. Li, S. Wang, K. Zhou, Q. Tan, and H. Feng, "Mechanical Behavior of Hinge Lozenge Grid Structure," in *IOP Conference Series: Materials Science and Engineering*, IOP Publishing, 2019, p. 12131.
[7] S.K. Bhullar, A.T.M. Hewage, A. Alderson, K. Alderson, M.B.G. Jun, Influence of negative Poisson's ratio on stent applications, Adv. Mater 2 (3) (2013) 42–47.
[8] F. Amin, M.N. Ali, U. Ansari, M. Mir, M.A. Minhas, W. Shahid, Auxetic coronary stent endoprosthesis: Fabrication and structural analysis, J Appl Biomater Funct Mater 13 (2) (2015) 127–135.
[9] S.K. Bhullar, J. Ko, Y. Cho, M.B.G. Jun, Fabrication and characterization of nonwoven auxetic polymer stent, Polym Plast Technol Eng 54 (15) (2015) 1553–1559.
[10] W. Wu, X. Song, J. Liang, R. Xia, G. Qian, D. Fang, Mechanical properties of anti-tetrachiral auxetic stents, Compos Struct 185 (2018) 381–392.
[11] L. Gu, S. Zhao, S.R. Froemming, Arterial wall mechanics and clinical implications after coronary stenting: comparisons of three stent designs, Int J Appl Mech 4 (02) (2012) 1250013.
[12] A. Kastrati, et al., Restenosis after coronary placement of various stent types, Am J Cardiol 87 (1) (2001) 34–39.
[13] R. Hamzehei, A. Serjouei, N. Wu, A. Zolfagharian, M. Bodaghi, 4D Metamaterials with Zero Poisson's Ratio, Shape Recovery, and Energy Absorption Features, Adv Eng Mater 24 (9) (2022) 2200656.
[14] R. Hamzehei, A. Zolfagharian, S. Dariushi, M. Bodaghi, 3D-printed bio-inspired zero Poisson's ratio graded metamaterials with high energy absorption performance, Smart Mater Struct 31 (3) (2022), 035001.
[15] R. Hamzehei, et al., Parrot Beak-Inspired metamaterials with friction and interlocking mechanisms 3D/4D printed in micro and macro scales for supreme energy absorption/dissipation, Adv Eng Mater (2023) 2201842.
[16] R. Hamzehei, J. Kadkhodapour, A.P. Anaraki, S. Rezaei, S. Dariushi, A. M. Rezadoust, Octagonal auxetic metamaterials with hyperelastic properties for large compressive deformation, Int J Mech Sci 145 (2018) 96–105.
[17] K.W. Wojciechowski, Two-dimensional isotropic system with a negative Poisson ratio, Phys Lett A 137 (1–2) (1989) 60–64.
[18] W. Wu, M. Qi, X.-P. Liu, D.-Z. Yang, W.-Q. Wang, Delivery and release of nitinol stent in carotid artery and their interactions: a finite element analysis, J Biomech 40 (13) (2007) 3034–3040.
[19] L.H. Timmins, M.W. Miller, F.J. Clubb, J.E. Moore, Increased artery wall stress post-stenting leads to greater intimal thickening, Laboratory Investigation 91 (6) (2011) 955–967.
[20] C. Dumoulin, B. Cochelin, Mechanical behaviour modelling of balloon-expandable stents, J Biomech 33 (11) (2000) 1461–1470.
[21] R. Critchley, I. Corni, J.A. Wharton, F.C. Walsh, R.J.K. Wood, K.R. Stokes, "A review of the manufacture, mechanical properties and potential applications of auxetic foams", Physica Status Solidi (b) 250 (10) (2013) 1963–1982.
[22] A. Bezazi, F. Scarpa, Tensile fatigue of conventional and negative Poisson's ratio open cell PU foams, Int J Fatigue 31 (3) (2009) 488–494.
[23] M. Sadegh Ebrahimi, R. Hashemi, and E. Etemadi, "In-plane energy absorption characteristics and mechanical properties of 3D printed novel hybrid cellular structures," *Journal of Materials Research and Technology*, vol. 20, pp. 3616–3632, Sep. 2022, doi: 10.1016/J.JMRT.2022.08.064.
[24] H. Xue, Z. Luo, T. Brown, S. Beier, Design of self-expanding auxetic stents using topology optimization, Front Bioeng Biotechnol 8 (2020) 736.
[25] G.E. Stavroulakis, Auxetic behaviour: appearance and engineering applications, Physica Status Solidi (b) 242 (3) (2005) 710–720.
[26] N. Wang, Auxetic nuclei, Nat Mater 13 (6) (2014) 540–542.
[27] T. Li, F. Liu, L. Wang, Enhancing indentation and impact resistance in auxetic composite materials, Compos B Eng 198 (2020), 108229.
[28] J. P. Donoghue, K. L. Alderson, and K. E. Evans, "The fracture toughness of composite laminates with a negative Poisson's ratio," *physica status solidi (b)*, vol. 246, no. 9, pp. 2011–2017, 2009.
[29] J. Zhang, G. Lu, Z. You, Large deformation and energy absorption of additively manufactured auxetic materials and structures: A review, Compos B Eng 201 (2020), 108340.
[30] N. Novak, O. Duncan, T. Allen, A. Alderson, M. Vesenjak, Z. Ren, Shear modulus of conventional and auxetic open-cell foam, Mechanics of Materials 157 (2021), 103818.
[31] M. Sanami, N. Ravirala, K. Alderson, A. Alderson, Auxetic materials for sports applications, Procedia Eng 72 (2014) 453–458.
[32] P. Mardling, A. Alderson, N. Jordan-Mahy, C.L. Le Maitre, The use of auxetic materials in tissue engineering, Biomater Sci 8 (8) (2020) 2074–2083.
[33] S.K. Bhullar, et al., Design and fabrication of auxetic PCL nanofiber membranes for biomedical applications, Materials Science and Engineering: C 81 (2017) 334–340.
[34] F. Scarpa, Auxetic materials for bioprostheses [In the Spotlight], IEEE Signal Process Mag 25 (5) (2008) 126–128.
[35] O. Abdelaal, S. Darwish, Analysis, fabrication and a biomedical application of auxetic cellular structures, Int. J. Eng. Innov. Technol 2 (3) (2012) 218–223.
[36] K.E. Evans, A. Alderson, Auxetic materials: functional materials and structures from lateral thinking!, Advanced Materials 12 (9) (2000) 617–628.
[37] R. Gatt, et al., Hierarchical auxetic mechanical metamaterials, Sci Rep 5 (1) (2015) 1–6.
[38] H.M.A. Kolken, S. Janbaz, S.M.A. Leeflang, K. Lietaert, H.H. Weinans, A. A. Zadpoor, Rationally designed meta-implants: A combination of auxetic and conventional meta-biomaterials, Mater Horiz 5 (1) (2018) 28–35.
[39] A.A. Zadpoor, Meta-biomaterials, Biomater Sci 8 (1) (2020) 18–38.
[40] X.L. Ruan, et al., Mechanical design of antichiral-reentrant hybrid intravascular stent, Int J Appl Mech 10 (10) (2018) 1850105.
[41] H. Li, Y. Ma, W. Wen, W. Wu, H. Lei, D. Fang, In plane mechanical properties of tetrachiral and antitetrachiral hybrid metastructures, J Appl Mech 84 (8) (2017) pp.
[42] X. Ren, J. Shen, A. Ghaedizadeh, H. Tian, Y.M. Xie, A simple auxetic tubular structure with tuneable mechanical properties, Smart Mater Struct 25 (6) (2016) 65012.
[43] K. Kuribayashi, et al., Self-deployable origami stent grafts as a biomedical application of Ni-rich TiNi shape memory alloy foil, Materials Science and Engineering: A 419 (1–2) (2006) 131–137.
[44] L. Mizzi, D. Attard, A. Casha, J.N. Grima, R. Gatt, On the suitability of hexagonal honeycombs as stent geometries, Physica Status Solidi (b) 251 (2) (2014) 328–337.
[45] R. Hamzehei, S. Rezaei, J. Kadkhodapour, A.P. Anaraki, A. Mahmoudi, 2D triangular anti-trichiral structures and auxetic stents with symmetric shrinkage behavior and high energy absorption, Mechanics of Materials 142 (2020), 103291.
[46] H.M.A. Kolken, A.A. Zadpoor, Auxetic mechanical metamaterials, RSC Adv 7 (9) (2017) 5111–5129.
[47] W. Liu, H. Li, Z. Yang, J. Zhang, X. Ge, In-plane elastic properties of a 2D chiral cellular structure with V-shaped wings, Eng Struct 210 (2020), 110384.
[48] C.W. Smith, J.N. Grima, K. Evans, A novel mechanism for generating auxetic behaviour in reticulated foams: missing rib foam model, Acta Mater 48 (17) (2000) 4349–4356.

[49] Y. Zhu, S. Jiang, L.H. Poh, Y. Shao, Q. Wang, Enhanced hexa-missing rib auxetics for achieving targeted constant NPR and in-plane isotropy at finite deformation, Smart Mater Struct 29 (4) (2020), 045030.
[50] J. Liu, Y. Zhang, Soft network materials with isotropic negative Poisson's ratios over large strains, Soft Matter 14 (5) (2018) 693–703.
[51] Y. Zhu, S. Jiang, J. Li, D.K. Pokkalla, Q. Wang, C. Zhang, Novel isotropic anti-tri-missing rib auxetics with prescribed in-plane mechanical properties over large deformations, Int J Appl Mech 13 (10) (2021) 2150115.
[52] M. Abbaslou, R. Hashemi, E. Etemadi, Novel hybrid 3D-printed auxetic vascular stent based on re-entrant and meta-trichiral unit cells: Finite element simulation with experimental verifications, Mater Today Commun 35 (2023), 105742, https://doi.org/10.1016/J.MTCOMM.2023.105742.
[53] D. Qi, et al., Innovative 3D chiral metamaterials under large deformation: Theoretical and experimental analysis, Int J Solids Struct 202 (2020) 787–797.
[54] D. Rahmatabadi, et al., Development of Pure Poly Vinyl Chloride (PVC) with Excellent 3D Printability and Macro-and Micro-Structural Properties, Macromol Mater Eng 308 (5) (2023) 2200568.
[55] E. Soleyman, et al., 4D printing of PET-G via FDM including tailormade excess third shape, Manuf Lett 33 (2022) 1–4.
[56] M. Moradi, A. Aminzadeh, D. Rahmatabadi, S.A. Rasouli, Statistical and experimental analysis of process parameters of 3d nylon printed parts by fused deposition modeling: Response surface modeling and optimization, J Mater Eng Perform 30 (7) (2021) 5441–5454.
[57] "In-plane mechanical behavior of novel auxetic hybrid metamaterials," *Thin-Walled Structures*, vol. 159, p. 107191, Feb. 2021, doi: 10.1016/J.TWS.2020.107191.
[58] X. Ruan, W. Yuan, Y. Hu, J. Li, W. Wu, R. Xia, Chiral constrained stent: Effect of structural design on the mechanical and intravascular stent deployment performances, Mechanics of Materials 148 (2020), 103509, https://doi.org/10.1016/J.MECHMAT.2020.103509.